



Aqueous electrolyte design for super-stable 2.5 V $\text{LiMn}_2\text{O}_4 \parallel \text{Li}_4\text{Ti}_5\text{O}_{12}$ pouch cells

Jijian Xu^{1,2}, Xiao Ji^{1,2}, Jiaxun Zhang¹, Chongyin Yang¹, Pengfei Wang¹, Sufu Liu¹, Kyle Ludwig¹, Fu Chen¹, Peter Kofinas¹ and Chunsheng Wang¹✉

To compete with commercial organic electrolytes, aqueous electrolytes beyond water-in-salt electrolytes with a lower salt concentration of $<5.0 \text{ m (mol kg}_{\text{solvent}}^{-1})$ and wider electrochemical stability window of $>3.0 \text{ V}$ are urgently needed. Here we report a 4.5 m lithium bis(trifluoromethanesulfonyl) imide (LiTFSI)-KOH- $\text{CO}(\text{NH}_2)_2\text{-H}_2\text{O}$ non-flammable ternary eutectic electrolyte that expands the electrochemical stability window to $>3.3 \text{ V}$ by forming a robust solid-electrolyte interphase. The ternary eutectic electrolyte enables $\text{Li}_{1.5}\text{Mn}_2\text{O}_4 \parallel \text{Li}_4\text{Ti}_5\text{O}_{12}$ pouch cells to achieve a high average Coulombic efficiency of 99.96% and capacity retention of 92% after 470 cycles at an areal capacity of 2.5 mAh cm^{-2} , a low positive/negative capacity ratio of 1.14 and a lean electrolyte (3 g Ah^{-1}). The Li loss due to the solid-electrolyte interphase formation in the initial charge/discharge cycles is compensated by an excess 0.5 Li in the $\text{Li}_{1.5}\text{Mn}_2\text{O}_4$ cathode, which converts the $\text{Li}_{1.5}\text{Mn}_2\text{O}_4 \parallel \text{Li}_4\text{Ti}_5\text{O}_{12}$ cell into $\text{LiMn}_2\text{O}_4 \parallel \text{Li}_4\text{Ti}_5\text{O}_{12}$ after solid-electrolyte interphase formation. The 2.5 V aqueous $\text{Li}_{1.5}\text{Mn}_2\text{O}_4 \parallel \text{Li}_4\text{Ti}_5\text{O}_{12}$ pouch cells with practical settings demonstrate a promising approach towards safe, low-cost and high-energy aqueous Li-ion batteries.

The recent concept of ‘solvent-in-salt’ electrolytes, namely ‘water-in-salt’ electrolytes (WISE) for aqueous batteries¹ and ‘super-concentrated’ electrolytes for non-aqueous batteries^{2–4}, greatly expands the electrochemical window of these battery systems and consequently their energy density. This expansion occurs because the large number of salt aggregates in ‘solvent-in-salt’ electrolytes enables preferential salt decomposition over solvent decomposition to form robust interphase layers on electrodes, thus enhancing their stability in a wide range of operating voltages^{5–9}.

For aqueous electrolytes, extensive efforts have also been made to further expand the electrochemical stability window of WISE by reducing H_2O molecules in the Li-ion solvation sheath by increasing the salt concentration to $27.7 \text{ m (mol kg}_{\text{solvent}}^{-1})$ in a hydrate melt electrolyte¹⁰, 28 m in a ‘water-in-bisalt’ electrolyte¹¹ with additives¹², 40 m in mixed cation electrolytes¹³, 55.5 m in a lithium-salt monohydrate¹⁴ and 63 m in ionic-liquid WISE¹⁵. However, even when the salt concentration reached 63 m , regardless of cost, the cathodic potential of the WISE expanded only to 1.75 V with an overall electrochemical stability window of $<3.25 \text{ V}$ (ref. ¹⁵). Although the increase in the salt concentration decreased the H_2O molecules’ solvation number, it did not suppress the water reduction. The Li-ion-solvated water will be reduced and the formed solid-electrolyte interphase (SEI) will wash out if the SEI is not robust enough to desolvate the water from the Li ion¹⁶. Alternatively, adding organic solvents^{17,18}, or gel polymers^{19–21}, that are capable of dissolving a large amount of both salt and solvent is a simple strategy to decrease the amount of water in WISE. However, these organic solvents—gel polymers—are also flammable, which compromises the merit of aqueous electrolytes. Up to now, it has seemed impossible to further deplete H_2O molecules within the Li-ion solvation sheath via a super-concentration strategy because of the limit of the lithium salts’ precipitation/dissolution equilibrium.

To design the next generation of dilute aqueous electrolytes beyond WISE, electrolytes that possess a wider electrochemical stability window and lower cost but still maintain the merit of

non-flammability, the diluent aqueous electrolytes have to satisfy three criteria. First, both the lithium salts and diluents must be able to form a robust SEI so that the cathodic limiting potential can be decreased to $<1.5 \text{ V}$ for $\text{Li}_4\text{Ti}_5\text{O}_{12}$ anodes. Second, diluents must be capable of forming a ternary eutectic with salts and H_2O to simultaneously achieve both a high ionic conductivity of $>10^{-3} \text{ S cm}^{-1}$ and a low viscosity. Third, diluents must be cheap and non-flammable.

Herein, by using $\text{CO}(\text{NH}_2)_2$ as a model diluent, we reported a non-flammable ternary eutectic electrolyte that fulfills all three requirements. The 4.5 m LiTFSI-KOH- $\text{CO}(\text{NH}_2)_2\text{-H}_2\text{O}$ aqueous electrolyte expanded the electrochemical stability window to 3.3 V with the cathodic limiting potential to 1.5 V , where $\text{CO}(\text{NH}_2)_2$ further decreased the number of H_2O in the Li^+ solvation shell from 2.6 in WISE to 0.7, and the reduction of LiTFSI and $\text{CO}(\text{NH}_2)_2$ under KOH catalyst formed a robust LiF/polymer bilayer SEI²². The 4.5 m LiTFSI-KOH- $\text{CO}(\text{NH}_2)_2\text{-H}_2\text{O}$ aqueous electrolyte at a lean amount of 3 g Ah^{-1} enabled $\text{Li}_{1.5}\text{Mn}_2\text{O}_4 \parallel \text{Li}_4\text{Ti}_5\text{O}_{12}$ pouch cells with thick electrodes of 2.5 mAh cm^{-2} , and a positive/negative (P/N) ratio of 1.14, to maintain 92% of the initial capacity after 470 charge/discharge cycles. The Li loss during the formation of the SEI was compensated by the extra 0.5 Li in $\text{Li}_{1.5}\text{Mn}_2\text{O}_4$, which converted the $\text{Li}_{1.5}\text{Mn}_2\text{O}_4 \parallel \text{Li}_4\text{Ti}_5\text{O}_{12}$ cells into regular $\text{LiMn}_2\text{O}_4 \parallel \text{Li}_4\text{Ti}_5\text{O}_{12}$ after SEI formation and notably enhanced the cycling life without hurting the cell energy density.

Solvation structure of 4.5 m electrolytes

All the $\text{CO}(\text{NH}_2)_2\text{-H}_2\text{O}$, $\text{CO}(\text{NH}_2)_2\text{-LiTFSI}$ and $\text{H}_2\text{O-LiTFSI}$ binary mixtures possess a eutectic composition (Supplementary Fig. 1a–c); the non-flammable $\text{CO}(\text{NH}_2)_2\text{-LiTFSI-H}_2\text{O}$ ternary eutectic electrolytes can potentially achieve a high ionic conductivity and a low viscosity. In addition, the bonding between $\text{CO}(\text{NH}_2)_2$ and H_2O is even stronger than bonds between H_2O molecules²³, and $\text{CO}(\text{NH}_2)_2$ can also promote the formation of a robust SEI layer in aqueous electrolyte and reduce the electrolyte viscosity^{24–26}. We first identify the liquid phase region in the mole triangle phase

¹Department of Chemical and Biomolecular Engineering, University of Maryland, College Park, MD, USA. ²These authors contributed equally: Jijian Xu, Xiao Ji. ✉e-mail: cswang@umd.edu

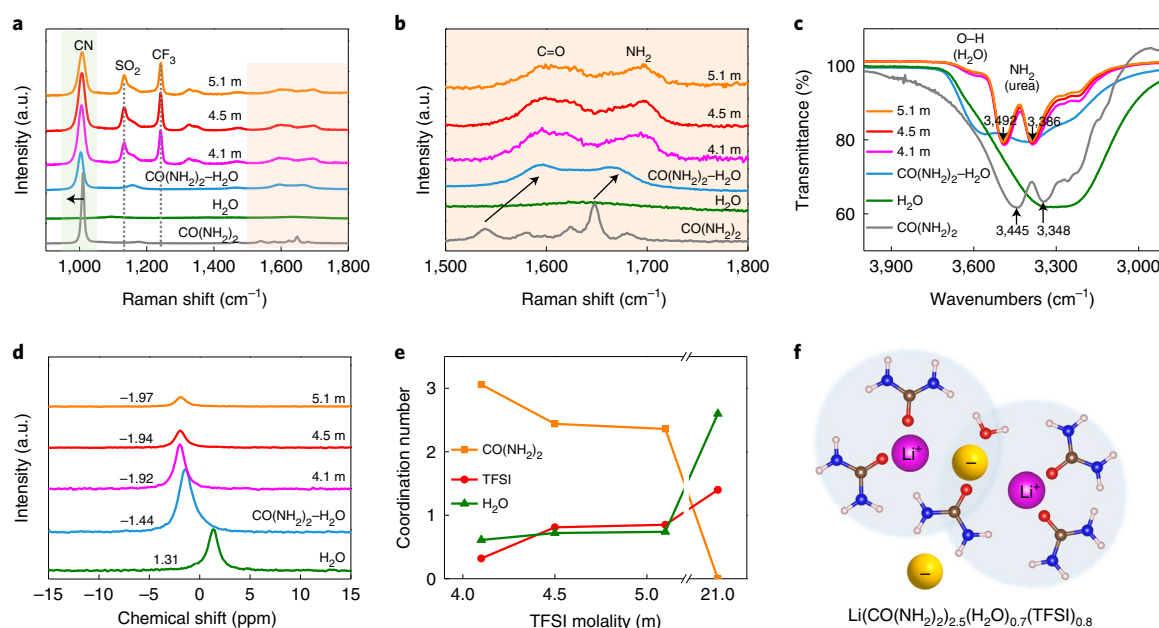


Fig. 1 | Spectrum analysis of intermolecular interaction. **a–c**, Raman spectra (**a,b**) and FTIR spectra (**c**) of the CO(NH₂)₂, H₂O, CO(NH₂)₂-H₂O, 4.1 m, 4.5 m and 5.1 m electrolytes. Enlargement of the shaded area in **a** that is shown in **b** is in the range of 1,500–1,800 cm⁻¹. The arrows in **c** indicate the shift in wavenumber. **d**, The chemical shift of ¹⁷O NMR in different electrolytes. **e**, Coordination numbers of CO(NH₂)₂, TFSI and H₂O around Li⁺ (within 3.0 Å) for the 4.1 m, 4.5 m and 5.1 m electrolytes compared with 21 m WISE. **f**, Illustration of the Li⁺ primary solvation shell in the 4.5 m electrolyte (H, rose red; Li, purple; C, brown; N, blue; O, red; TFSI, orange).

diagram with all the compositions marked, as shown in Supplementary Fig. 1d, by focusing on the area near to the ternary eutectic composition. At the ternary eutectic composition region of LiTFSI-CO(NH₂)₂-H₂O electrolyte, we selected 4.1 m, 4.5 m and 5.1 m electrolytes (Supplementary Table 1) due to their high electrolyte stability window, viscosity and ionic conductivity (Supplementary Note 1).

The molecular interactions among LiTFSI, CO(NH₂)₂ and H₂O were first investigated by vibrational analysis and used as references. Figure 1a and Supplementary Fig. 2 display the Raman spectra of 4.1 m, 4.5 m, 5.1 m and eutectic CO(NH₂)₂-H₂O aqueous electrolytes along with those of individual CO(NH₂)₂ and H₂O (ref. 27). The intense Raman band at 1,010 cm⁻¹ in CO(NH₂)₂, corresponding to the symmetrical C–N stretching vibration, shifted to a lower wavenumber of 1,006 cm⁻¹ in the three aqueous electrolytes of CO(NH₂)₂-LiTFSI-H₂O-KOH (4.1 m, 4.5 m and 5.1 m) and shifted even lower to 1,004 cm⁻¹ in eutectic CO(NH₂)₂-H₂O solution. Because of the weakening of intramolecular hydrogen bonds, the C–N bond becomes longer, and the corresponding vibration shifts to a lower wavenumber²⁸. The strong interaction between H₂O and CO(NH₂)₂ was also reflected by the shift of the C=O and NH₂ modes (Fig. 1b). According to Keuleers²⁹, the band at 1,647 cm⁻¹ mainly reflects NH₂ deformation, while the band at a lower frequency (1,540 cm⁻¹) has more C=O character (Supplementary Note 2). Apparently, both NH₂ deformation and C=O wagging vibrations in the eutectic CO(NH₂)₂-H₂O solution shift to a higher frequency due to the increase of hydrogen bonding strength via CO(NH₂)₂-H₂O intermolecular interaction. An even larger shift occurs in the three electrolytes upon the addition of LiTFSI due to the strong interaction of LiTFSI and H₂O. Therefore, both LiTFSI and CO(NH₂)₂ can decrease H₂O activity and stabilize the H₂O.

The strong CO(NH₂)₂-H₂O interactions in the 4.1 m, 4.5 m and 5.1 m electrolytes were also confirmed using Fourier transform infrared spectroscopy (FTIR). As shown in Fig. 1c, the two strong bands of CO(NH₂)₂ at 3,348 and 3,445 cm⁻¹ can be assigned to the

NH₂ stretching vibrations. These two NH₂ stretching vibrations shift to a higher frequency in the 4.1 m, 4.5 m and 5.1 m aqueous electrolytes due to stronger hydrogen bonding²⁹. Furthermore, a visible band at ~3,600 cm⁻¹ appeared in the three aqueous electrolytes (4.1 m, 4.5 m and 5.1 m), while H₂O only has a characteristic broad band at 2,900–3,700 cm⁻¹. This new band was also found in eutectic CO(NH₂)₂-H₂O with higher intensity, suggesting that isolated H₂O interacted with CO(NH₂)₂, which is in line with a previous report²⁵.

The ¹⁷O nuclear magnetic resonance (NMR) spectra also confirmed the strong bonding between CO(NH₂)₂ and H₂O (Fig. 1d). The ¹⁷O signal at 1.31 ppm for bulk H₂O is negatively shifted by -2.75 to -1.44 ppm when 50% of CO(NH₂)₂ was added into H₂O, forming a eutectic solution, suggesting extensive interactions between H₂O and CO(NH₂)₂ (ref. 30). When 4.1 m, 4.5 m and 5.1 m LiTFSI were added to the electrolytes, the ¹⁷O signal further shifted by -0.48, -0.5 and -0.53, respectively, demonstrating that H₂O interacts with CO(NH₂)₂ more strongly than with Li⁺. However, the ¹⁷O signal shift with increasing salt concentration is small because of the equilibrium of LiTFSI dissociation, which is confirmed by the negligible shift of the characteristic Raman band of TFSI (744.5 cm⁻¹) as the salt concentration increases (Supplementary Fig. 2). This result indicates that CO(NH₂)₂ can more strongly stabilize the H₂O than LiTFSI salt can. Therefore, CO(NH₂)₂ can replace LiTFSI to stabilize H₂O, thus reducing the salt concentration.

The solvation structures of the electrolytes were simulated using molecular dynamics (Methods). The equilibrated systems of the 4.1 m, 4.5 m and 5.1 m electrolytes are shown in Supplementary Fig. 3. The introduction of CO(NH₂)₂ into LiTFSI-H₂O electrolytes largely changes the structure of the primary Li⁺ solvation sheath. Figure 1e and Supplementary Fig. 4 summarize the coordination numbers and pair distribution functions of the 4.1 m, 4.5 m and 5.1 m electrolytes. In the 4.1 m electrolyte, each Li⁺ is on average surrounded by 3.1 CO(NH₂)₂, 0.3 TFSI and only 0.6 H₂O, which is less than the 2.6 H₂O in each Li⁺ primary solvation sheath in the 21 m WISE¹. CO(NH₂)₂ can act as an additional Li⁺ ion coordinate

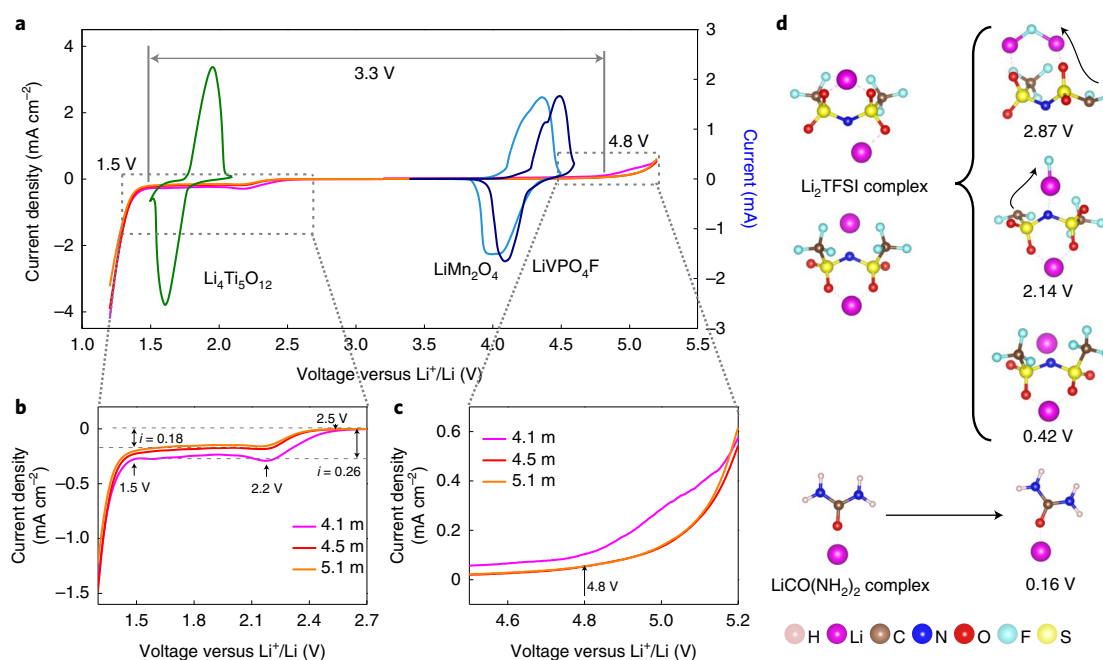


Fig. 2 | The electrochemical stability window of aqueous electrolytes. **a**, Overall electrochemical stability window of the electrolytes with different LiTFSI concentrations, and redox of electrodes overlaid with cyclic voltammograms on current collectors. The redox currents of active electrodes (Li₄Ti₅O₁₂, LiMn₂O₄ and LiVPO₄F) in 4.5 m electrolytes were measured using a cyclic voltammogram at a scanning rate of 0.2 mV s⁻¹. **b, c**, The enlarged view of the regions outlined near the cathodic (**b**) and anodic (**c**) extremes in **a**. *i*, current density. **d**, Predicted reduction potential (voltage versus Li/Li⁺) via quantum chemistry calculations.

site and consequently replace water in the Li⁺ primary solvation shell, which is consistent with the spectroscopic results (Fig. 1d)³¹. The 4.5 m and 5.1 m electrolytes share almost the same Li⁺ primary solvation structure. However, the coordination numbers of TFSI increase with the LiTFSI concentration from 0.81 in 4.5 m to 0.85 in 5.1 m. The 4.5 m electrolyte corresponds to a (Li(CO(NH₂)₂)_{2.5}(H₂O)_{0.7}(TFSI)_{0.8}) solvation structure (Fig. 1f). In addition, hydrogen bonding between CO(NH₂)₂ and H₂O can be clearly observed, according to the molecular dynamics simulations (Supplementary Fig. 5), which decreases the H₂O activity. Therefore, the addition of CO(NH₂)₂ can minimize the interfacial H₂O on the anode surface and suppress the H₂O activity, thus expanding the electrochemical stability window. A small amount of KOH was added simultaneously with CO(NH₂)₂ to catalyse the reduction of the TFSI, forming a LiF-rich SEI.

Electrochemical properties of 4.5 m electrolytes

The electrochemical stability windows of the 4.1 m, 4.5 m and 5.1 m aqueous electrolytes were evaluated by linear sweep voltammetry at a scanning rate of 0.2 mV s⁻¹ (Fig. 2). The electrolyte stability windows of the three electrolytes extend notably from 3.0 V of WISE to 3.3 V, and the cathodic potential negatively shifts by 0.4 V from 1.9 V to 1.5 V (Fig. 2a). Figure 2b indicates that the reduction at all concentrations starts at ~2.5 V (before the cathodic limit of 2.4 V, according to the Pourbaix diagram of water at pH 10) and reaches a plateau at ~2.2 V. The fluorinated lithium salt (LiTFSI) plays an important role in forming a LiF-rich SEI¹⁰. Density functional theory calculations (Fig. 2d) also demonstrate that the reduction potential of LiTFSI is much higher than that of CO(NH₂)₂, suggesting the preferential reduction of LiTFSI over CO(NH₂)₂. KOH further accelerates the reduction kinetics of LiTFSI (Supplementary Fig. 6 and Supplementary Note 3).

The high solubilization ability of CO(NH₂)₂ results in inter-phase chemistry dominated by CO(NH₂)₂ rather than by H₂O.

A synergistic effect among LiTFSI, CO(NH₂)₂ and KOH contributes to a robust SEI layer, which successfully pushes the cathodic limit to 1.5 V. Linear sweep voltammetry curves of the dilute 4.1 m electrolyte show a slightly large plateau current of 0.26 mA cm⁻² compared to 0.18 mA cm⁻² for the 4.5 m or 5.1 m electrolytes, and a slightly higher anodic current than those of the 4.5 m or 5.1 m electrolytes (Fig. 2c). Overall, a widened electrochemical window of 3.3 V is achieved for the aqueous electrolyte of 4.5 m LiTFSI–KOH–CO(NH₂)₂–H₂O, although 4.5 m aqueous electrolytes show a slightly lower anodic limitation (4.8 V) than that of WISE (4.9 V) due to the CO(NH₂)₂ oxidation reaction occurring, rather than Al corrosion (Supplementary Figs. 7 and 8 and Supplementary Note 4)³².

The cyclic voltammogram of the Li₄Ti₅O₁₂, LiMn₂O₄ and LiVPO₄F electrodes in 4.5 m electrolyte show the characteristic redox peaks (Fig. 2a), which are all shifted upward by about 0.2 V due to the Nernst shift. Li₄Ti₅O₁₂ with its fast reaction kinetics and long cycling stability has been excluded in previous aqueous electrolytes because of the ‘cathodic challenge’ (~1.7–1.9 V versus Li/Li⁺). Previous strategies, such as using an extremely high concentration of 63 m with gel passivation¹⁵ or adding poly(ethylene glycol) PEG in aqueous electrolytes along with a Li_{1.3}Al_{0.3}Ti_{1.7}(PO₄)₃ coating on Li₄Ti₅O₁₂ (ref. 21), still cannot achieve the Coulombic efficiency (>99.9%) required for commercialization of Li₄Ti₅O₁₂ anodes in aqueous Li-ion batteries. Up to now, LiMn₂O₄||Li₄Ti₅O₁₂ full cells with a practical loading of active materials (~2.5 mAh cm⁻²) and a low cathode excess (<15%) still cannot operate for a long cycle life (Table 1).

The SEI layers on Li₄Ti₅O₁₂ electrodes after cycling in 4.5 m aqueous electrolytes were characterized using X-ray photoelectron spectroscopy (XPS) and time-of-flight secondary-ion mass spectrometry. Figure 3 displays the C 1s (Fig. 3a), N 1s (Fig. 3b), O 1s (Fig. 3c) and F 1s (Fig. 3d) XPS core peaks of cycled Li₄Ti₅O₁₂ electrodes. The characteristic C 1s peak located at 284.2 eV derives from conductive carbon, and the CF₃ peak at 293.0 eV comes

Table 1 | Comparison of 4.5 m electrolyte with other reported electrolytes for $\text{Li}_4\text{Ti}_5\text{O}_{12}$ -based aqueous Li-ion batteries

Electrolyte composition	Areal capacity (mAh cm^{-2})	P/N ratio	Cycle life at 1 C	Flammability	Reference
27.7 m LiTFSI-BETI	0.22	2	200 (75%)	Non	10
2 m LiTFSI-PEG	0.25	0.6	300 (68%)	Low	21
15.3 m LiTFSI- CH_3CN	0.32	1.9	300 (98%)	Low	18
63 m Me_3EtN -LiTFSI	0.5	1.1	100 (88%)	Non	15
4.5 m LiTFSI-KOH- $\text{CO}(\text{NH}_2)_2$	1.5	1.14	1,000 (88%)	Non	This work
4.5 m LiTFSI-KOH- $\text{CO}(\text{NH}_2)_2$	2.5	1.14	470 (92%)	Non	This work

BETI, (bis(pentafluoroethanesulfonyl) imide).

from the polyvinylidene fluoride binder in the anode composites. The detected 286.1 eV signal in C 1s, 400.0 eV signal in N 1s and 232.6 eV signal in O 1s belong to organic C–O–N species derived by $\text{CO}(\text{NH}_2)_2$ (refs. 33,34). The presence of a minor amount of Li_2CO_3 as an SEI component is supported by the 290.5 eV signal in C 1s and 530.5 eV signal in O 1s spectra. The formation of Li_2CO_3 is attributed to CNO^- and then CO_3^{2-} that were formed by the decomposition of $\text{CO}(\text{NH}_2)_2$ through nucleophilic attack under alkaline conditions³⁵. Inorganic LiF is examined by the additional F 1s signal at 685.5 eV (Fig. 3d), which results from the reduction of LiTFSI. The residual F 1s signal at 688.5 eV can be assigned to the polyvinylidene fluoride binder. The XPS patterns of a $\text{Li}_4\text{Ti}_5\text{O}_{12}$ electrode before cycling were also measured for comparison. As shown in Supplementary Fig. 9, no obvious Li_2CO_3 or LiF signal was detected.

The spatial distribution of species in the SEI on the $\text{Li}_4\text{Ti}_5\text{O}_{12}$ surface was analysed by depth profiles of time-of-flight secondary-ion mass spectrometry (Supplementary Fig. 10 and Supplementary Note 5). Figure 3e shows the edge surface of the crater sputtered by Ga^+ ions with a depth of 1.3 μm . According to the concentration depth profiles in Fig. 3f, CN^- and F^- concentrations decrease quickly with the etching, whereas an obvious increase of the O^- concentration derived from $\text{Li}_4\text{Ti}_5\text{O}_{12}$ active material is observed. Closer examination shows that the concentration of LiF-related species (F^-) decrease with a lower concentration gradient than that of organic species (CN^-) from the surface to the bulk of the electrode, indicating that organic species are located mainly at the top surface, while LiF species are located more deeply in the surface layer. Note that the F^- signal intensity in the 4.5 m aqueous electrolytes without KOH additive (Supplementary Fig. 11) is lower compared with that from the SEI in 4.5 m aqueous electrolytes with KOH additive (Fig. 3f), which indicates that more LiF is generated with the KOH additive.

The structure of the cycled $\text{Li}_4\text{Ti}_5\text{O}_{12}$ electrodes was also characterized by high-resolution transmission electron microscopy, further verifying a LiF/polymer bilayer SEI in Fig. 3g. The polymer/LiF bilayer SEI on a cycled $\text{Li}_4\text{Ti}_5\text{O}_{12}$ surface in 4.5 m electrolyte is different from the crystalline LiF SEI formed on Mo_6S_8 in WISE¹¹. Together with the C–O–N species detected with XPS and the CN^- species detected with time-of-flight secondary-ion mass spectrometry, we ascribed the amorphous characteristics to polyurea³⁶. Thus, the SEI formed on the $\text{Li}_4\text{Ti}_5\text{O}_{12}$ anode surface during cycling in 4.5 m electrolyte is a mixture of organic species and inorganic species mainly consisting of LiF. In addition, the high-resolution transmission electron microscopy result also suggests the formation of a cathode electrolyte interface (CEI) layer on the LiMn_2O_4 cathode side (Supplementary Fig. 12).

From the SEI composition analysis, the possible mechanism for the SEI formation is summarized in Fig. 3h. First, TFSI generates F^- anions via a nucleophilic attack in the presence of OH^- (ref. 22). Under the alkaline conditions, F^- anions quickly precipitate with Li^+ cations, forming the inner LiF layer at a high potential,

while at a low potential, urea electrochemically polymerizes into polyurea³⁷ on the LiF outer surface. Such a robust bilayer SEI with a LiF-rich inner layer and organic outer layer is beneficial for stable performance³⁸.

Electrochemical performance of full cells

The $\text{Li}_4\text{Ti}_5\text{O}_{12}$ anode was paired with either a LiMn_2O_4 or LiVPO_4F cathode, forming a full cell with a low P/N capacity ratio of 1.14. A slight excess of cathode electrode capacity was used to counteract the irreversible lithium depletion during SEI formation. The detailed parameters of the electrodes are listed in the Supplementary Information, and typical scanning electron microscopy images of $\text{Li}_4\text{Ti}_5\text{O}_{12}$ and LiMn_2O_4 with 1.5 mAh cm^{-2} and 2.5 mAh cm^{-2} are presented in Supplementary Figs. 13 and 14, respectively.

The electrochemical performances of $\text{LiMn}_2\text{O}_4||\text{Li}_4\text{Ti}_5\text{O}_{12}$ full cells were evaluated in the 5.1 m, 4.5 m and 4.1 m electrolytes (Fig. 4a,b). The Coulombic efficiency at a low rate of 0.2C (C, charge current; 1C is one hour to fully charge) was applied to monitor any side reaction, a technique that is also used in the real battery environment³⁹. $\text{LiMn}_2\text{O}_4||\text{Li}_4\text{Ti}_5\text{O}_{12}$ full cells at an areal capacity of 1.5 mAh cm^{-2} in 5.1 m and 4.5 m electrolytes are relatively stable upon cycling, even at 0.2C and a low P/N value, while cell stability in the 4.5 m electrolyte is much better than that in the 4.1 m electrolyte (Fig. 4a). The slightly lower capacity of the full cell in the 5.1 m electrolyte than in the 4.5 m electrolyte is attributed to the higher viscosity caused by the increase of salt concentration (Supplementary Fig. 15). As shown in Fig. 4b, the Coulombic efficiencies of $\text{LiMn}_2\text{O}_4||\text{Li}_4\text{Ti}_5\text{O}_{12}$ full cells in the 4.1 m, 4.5 m and 5.1 m electrolytes are 82.6%, 90.7% and 92.8% in the first cycle, values that progressively increase in the subsequent cycles and finally stabilize at 99.0% (4.1 m), 99.7% (4.5 m) and 99.8% (5.1 m), respectively. Among the three electrolytes, the 4.5 m electrolyte has the best overall properties, that is, a relatively high ionic conductivity (1.0 mS cm^{-1} ; Supplementary Fig. 16), a low viscosity (0.32 Pa s), a wide electrochemical window (3.3 V), a low freezing temperature of -60°C and a high thermal stability of 225°C (Supplementary Fig. 17). Taking all these physicochemical properties and cost factors into consideration, the 4.5 m electrolyte is selected for further detailed study.

The 1.5 mAh cm^{-2} $\text{LiMn}_2\text{O}_4||\text{Li}_4\text{Ti}_5\text{O}_{12}$ full cells in 4.5 m electrolyte retain >87% capacity even after 1,000 cycles with a discharge capacity of 61.3 mAh g^{-1} , corresponding to an anode capacity of 154.6 mAh g^{-1} and cathode capacity of 101.6 mAh g^{-1} at 0.5C (Fig. 4c,d). The full cells demonstrate an initial Coulombic efficiency as high as 91.9% due to the formation of a highly insulated LiF-rich SEI. The Coulombic efficiencies increase to 99% within five cycles and ultimately achieve an average Coulombic efficiency of 99.96% after 26 cycles. By contrast, the $\text{LiMn}_2\text{O}_4||\text{Li}_4\text{Ti}_5\text{O}_{12}$ cells in 4.5 m electrolyte without KOH additive show a gradual capacity decay upon cycling, as shown in Supplementary Fig. 18. As mentioned

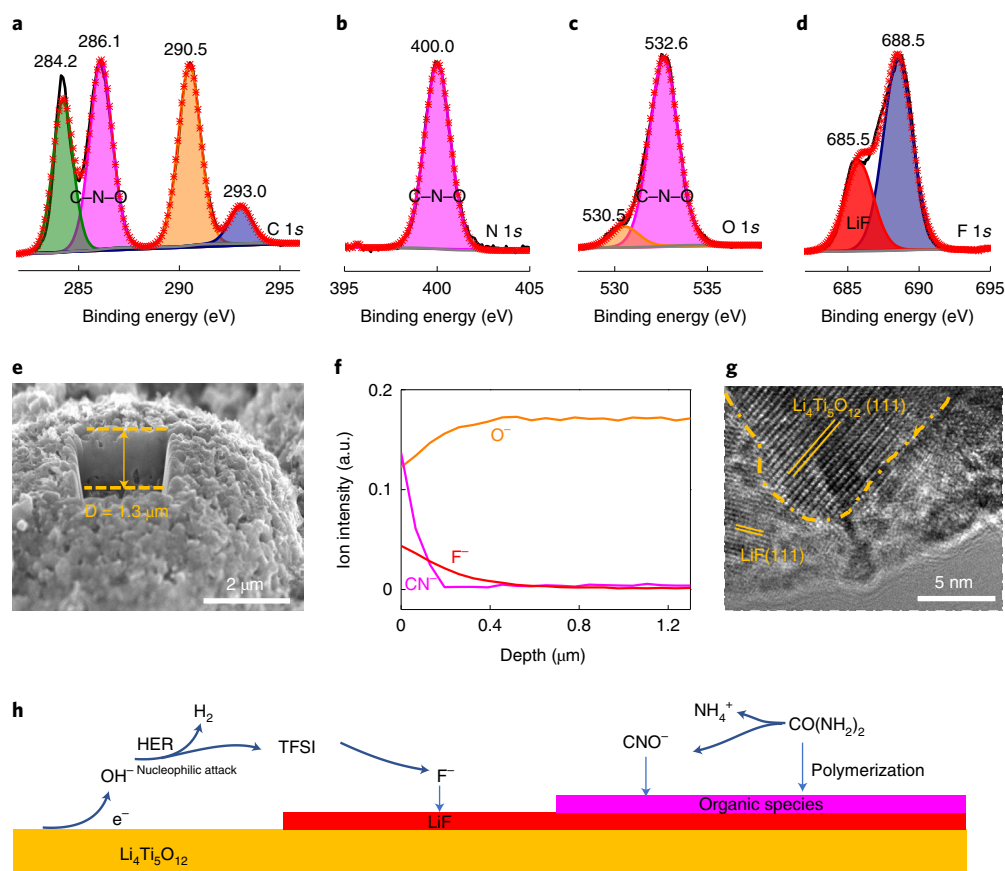


Fig. 3 | Structural and chemical analysis of SEI layer. a–d, XPS results for C 1s (**a**), N 1s (**b**), O 1s (**c**) and F 1s (**d**). **e,** Surface morphology of cycled $\text{Li}_4\text{Ti}_5\text{O}_{12}$ particles using 4.5 m electrolyte for time-of-flight secondary-ion mass spectrometry analysis over a $2 \times 2 \mu\text{m}^2$ raster size. **D,** depth. **f,** Time-of-flight secondary-ion mass spectrometry depth profiles of O^- , F^- and CN^- secondary ions on the cycled $\text{Li}_4\text{Ti}_5\text{O}_{12}$ particles. **g,** High-resolution transmission electron microscopy images of cycled $\text{Li}_4\text{Ti}_5\text{O}_{12}$ covered with a LiF/polymer bilayer SEI. **h,** Schematic illustration of the formation of the inorganic/organic mixed SEI. HER, hydrogen evolution reaction.

earlier, the universal electrolyte design strategy can be applied to other amides (for example, urea and *N*-methyl acetamide) with a similar molecular structure (Supplementary Fig. 19). By replacing urea with *N*-methyl acetamide, the $\text{LiMn}_2\text{O}_4 \parallel \text{Li}_4\text{Ti}_5\text{O}_{12}$ full cell also shows excellent stability with high capacity retention (90% with 450 cycles), as shown in Supplementary Fig. 20. The battery performance of a 2.6 V $\text{LiVPO}_4\text{F} \parallel \text{Li}_4\text{Ti}_5\text{O}_{12}$ full cell at P/N=1.14 was also cycled in 4.5 m aqueous electrolyte at the rate of 0.5C (Fig. 4e,f and Supplementary Note 6). The Coulombic efficiency of $\text{LiVPO}_4\text{F} \parallel \text{Li}_4\text{Ti}_5\text{O}_{12}$ full cells at a low rate of 0.2C is 82.1% in the first cycle, which gradually increases in the following cycles and finally stabilizes at around 99.2% (Supplementary Fig. 21).

$\text{LiMn}_2\text{O}_4 \parallel \text{Li}_4\text{Ti}_5\text{O}_{12}$ pouch cells with the same areal capacity of 1.5 mAh cm^{-2} and P/N capacity ratio of 1.14 exhibit an average Coulombic efficiency of 99.97% and retain 88% capacity after 1,000 cycles at 1C (Fig. 5a), which is a much better performance than that of other aqueous electrolytes reported to date (Table 1). The increase in areal capacity from 1.5 to 2.5 mAh cm^{-2} only slightly increases the overpotential, demonstrating the super performance of the 4.5 m electrolytes (Supplementary Fig. 22). After electro-osmotic wetting by holding the 2.5 mAh cm^{-2} $\text{LiMn}_2\text{O}_4 \parallel \text{Li}_4\text{Ti}_5\text{O}_{12}$ pouch cell at a voltage of 2.0 V for 12 h and applying an optimized external pressure of 0.5 MPa (Supplementary Fig. 23), the cell exhibits a high capacity retention of 72% after 500 cycles (Fig. 5b). The Coulombic efficiency in the first cycle at 1C is very high (93.6%) and quickly increases to 99.9% in 50 cycles, demonstrating that the formed SEI in the first few cycles effectively suppressed the water

decomposition. The average Coulombic efficiency from 10 to 500 cycles is 99.87%, which is comparable to that of organic electrolyte $\text{LiMn}_2\text{O}_4 \parallel \text{Li}_4\text{Ti}_5\text{O}_{12}$ cells. The initial capacity decay in Fig. 5b is probably attributed to the consumption of Li in LiMn_2O_4 during the formation of the SEI at a high overpotential.

To understand the initial capacity decay mechanism, three-electrode pouch cells with a $\text{Li}_{0.5}\text{FePO}_4$ -coated Al wire as a reference were used to simultaneously monitor the electrochemical behaviours of a LiMn_2O_4 cathode and $\text{Li}_4\text{Ti}_5\text{O}_{12}$ anode at 1C in 4.5 m aqueous electrolytes. As shown in Supplementary Fig. 24, LiMn_2O_4 shows a faster capacity decay than that of $\text{Li}_4\text{Ti}_5\text{O}_{12}$ due to the loss of lithium from LiMn_2O_4 in the formation of the SEI on $\text{Li}_4\text{Ti}_5\text{O}_{12}$. Since LiMn_2O_4 can be reversibly further lithiated into $\text{Li}_{1.5}\text{Mn}_2\text{O}_4$, the initial capacity decay of LiMn_2O_4 was completely removed by using lithium-rich $\text{Li}_{1.5}\text{Mn}_2\text{O}_4$ as cathodes, as demonstrated in Fig. 5c. The use of $\text{Li}_{1.5}\text{Mn}_2\text{O}_4$ to replace LiMn_2O_4 in $\text{Li}_{1.5}\text{Mn}_2\text{O}_4 \parallel \text{Li}_4\text{Ti}_5\text{O}_{12}$ cells can achieve super capacity stability in both the initial SEI formation cycles and following long-term cycles without hurting the cell energy density⁴⁰. The rate capability of the $\text{LiMn}_2\text{O}_4 \parallel \text{Li}_4\text{Ti}_5\text{O}_{12}$ pouch cells is presented in Supplementary Fig. 25, delivering reversible capacities of 58.6 (92%), 46.9 (74%) and 34.8 mAh g^{-1} (55%) at current densities of 1C, 2C and 3C, respectively.

The high cycling Coulombic efficiency occurs because the SEI completely avoided the water decomposition. Operando gas monitoring using pressure cells and gas chromatography (Supplementary Fig. 26) was conducted to analyse the gas release from $\text{LiMn}_2\text{O}_4 \parallel \text{Li}_4\text{Ti}_5\text{O}_{12}$ pouch cells in 4.5 m electrolyte. As shown

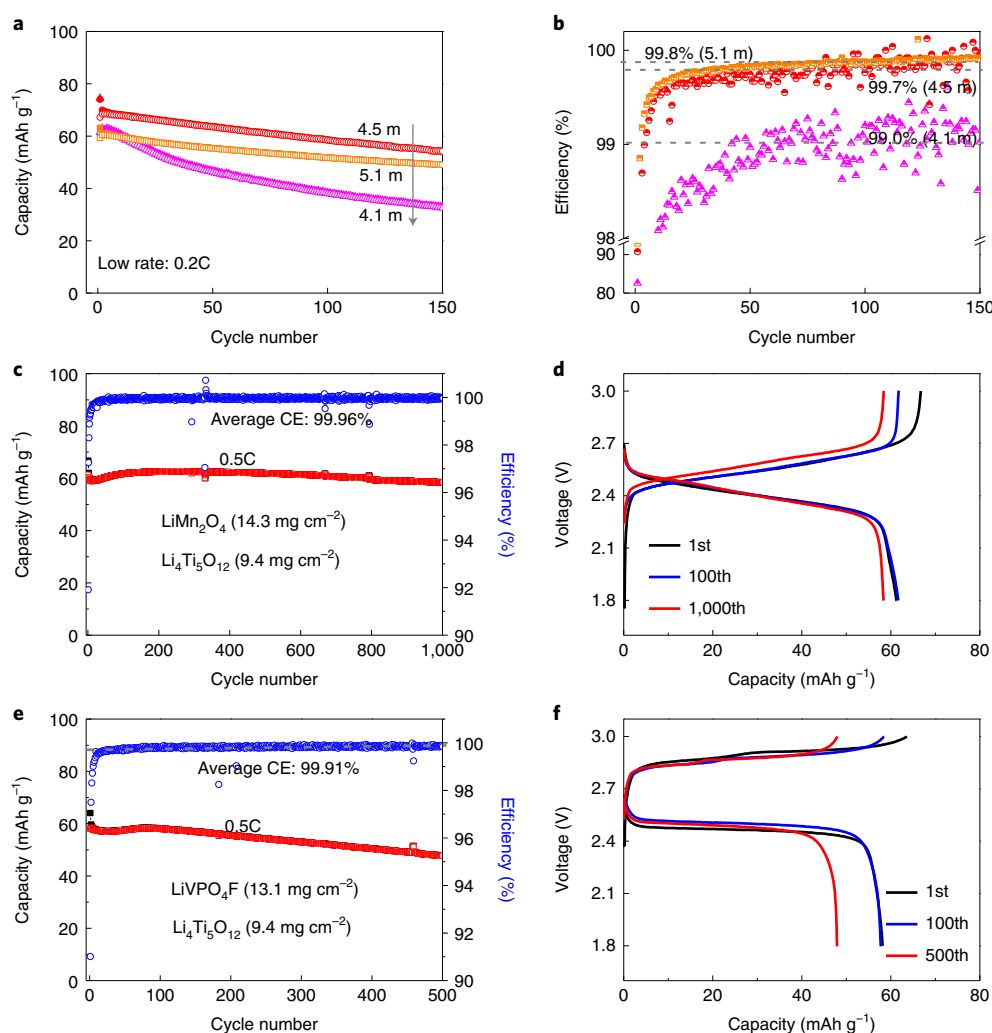


Fig. 4 | Electrochemical performances of 2.5 V $\text{LiMn}_2\text{O}_4 \parallel \text{Li}_4\text{Ti}_5\text{O}_{12}$ and 2.6 V $\text{LiVPO}_4\text{F} \parallel \text{Li}_4\text{Ti}_5\text{O}_{12}$ full cells at an areal capacity of 1.5 mAh cm^{-2} . **a,b**, Cycle performance (**a**) and the Coulombic efficiency (**b**) of the $\text{LiMn}_2\text{O}_4 \parallel \text{Li}_4\text{Ti}_5\text{O}_{12}$ full cell with $P/N=1.14$ in different aqueous electrolytes. **c,d**, The cycling stability (**c**) and the voltage profile (**d**) of the $\text{LiMn}_2\text{O}_4 \parallel \text{Li}_4\text{Ti}_5\text{O}_{12}$ full cell in 4.5 m electrolyte at 0.5C. CE, Coulombic efficiency. **e,f**, The cycling stability (**e**) and the voltage profile (**f**) of the $\text{LiVPO}_4\text{F} \parallel \text{Li}_4\text{Ti}_5\text{O}_{12}$ full cell in 4.5 m electrolyte at 0.5C. All the capacity values are based on the total electrode mass.

in Supplementary Fig. 27, gas generated at a high state of charge and the amount of gas released gradually decreased with charge/discharge cycles, and no detectable gas was released after 20 cycles, so the pressure kept constant. The released gas was H_2 , as demonstrated by gas chromatography. Therefore, the formed SEI in the first 20 cycles effectively inhibited the water reduction. Another critical challenge for aqueous batteries is the high self-discharge rate. The self-discharge rate with 18.7% of capacity decay per month for the lab-made 2.5 mAh cm^{-2} $\text{LiMn}_2\text{O}_4 \parallel \text{Li}_4\text{Ti}_5\text{O}_{12}$ pouch cell in 4.5 m aqueous electrolyte at room temperature is comparable with that of commercial (mature) nickel metal hydride (NiMH) batteries (20–30% per month). In addition, a lean electrolyte ($E/C=3 \text{ g Ah}^{-1}$, where E is the mass of the electrolyte and C is the capacity of the cell) $\text{LiMn}_2\text{O}_4 \parallel \text{Li}_4\text{Ti}_5\text{O}_{12}$ cell of 4.5 m aqueous electrolyte showed a similar or lower self-discharge rate than an identical $\text{LiMn}_2\text{O}_4 \parallel \text{Li}_4\text{Ti}_5\text{O}_{12}$ cell with 1.0 M electrolyte of LiPF_6 in ethylene carbonate and dimethyl carbonate at the same amount ($E/C=3 \text{ g Ah}^{-1}$) at 25°C (Supplementary Figs. 28 and 29). Moreover, a $\text{LiMn}_2\text{O}_4 \parallel \text{Li}_4\text{Ti}_5\text{O}_{12}$ cell in 4.5 m aqueous electrolyte showed a lower self-discharge rate than the identical $\text{LiMn}_2\text{O}_4 \parallel \text{Li}_4\text{Ti}_5\text{O}_{12}$ cell in 1.0 M electrolyte of LiPF_6 in ethylene carbonate and dimethyl carbonate at 55°C (Supplementary Figs. 30 and 31). Therefore, the 4.5 m aqueous

electrolyte enables the formation of a stable SEI, which successfully suppresses side reactions (H_2O decomposition in particular) even at a high temperature of 55°C .

The ternary eutectic electrolyte achieves an expanded electrochemical stability window of 3.3 V without using super-concentrated salts (Fig. 5d). According to the model of Betz and coworkers¹¹, an energy density of 103 Wh kg^{-1} for 2.5 mAh cm^{-2} aqueous $\text{LiMn}_2\text{O}_4 \parallel \text{Li}_4\text{Ti}_5\text{O}_{12}$ 18650-type cells is obtained, which is slightly higher than the best NiMH technology (100 Wh kg^{-1}), to the best of our knowledge. The cell energy density can be further enhanced to 123 Wh kg^{-1} if a high-capacity LiVPO_4F cathode is used to replace LiMn_2O_4 (ref. 18). All the specific energy densities from step 1 to step 6 are listed in Supplementary Table 2. Details for the calculation are presented in Supplementary Tables 3–5. The cost of cells is estimated by the following model as shown in Supplementary Fig. 32. The total cost of aqueous electrolyte $\text{LiMn}_2\text{O}_4 \parallel \text{Li}_4\text{Ti}_5\text{O}_{12}$ cells can reach US\$110 (Supplementary Fig. 33). Taking other factors, listed in Supplementary Table 6, into consideration, including voltage, rate capability, environmental friendliness and cycle life, it is reasonable to expect that such chemistry could outperform current commercial aqueous technologies including lead–acid, Ni–Cd and NiMH batteries (Fig. 5e)⁴².

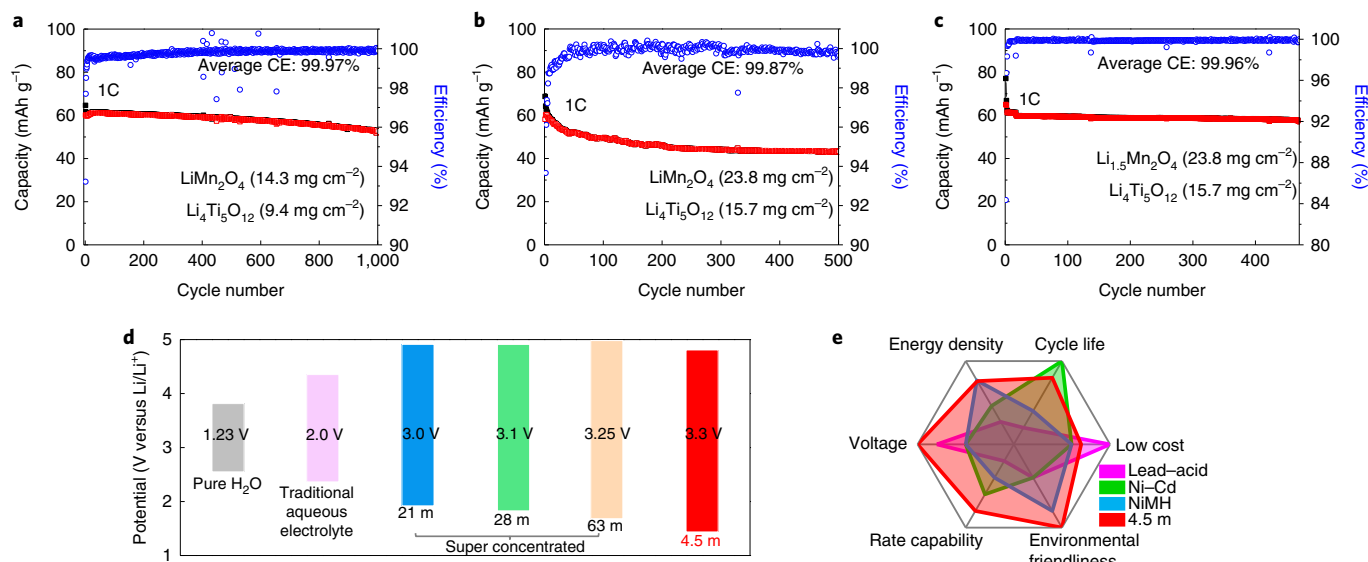


Fig. 5 | Electrochemical performances of 2.5 V $\text{LiMn}_2\text{O}_4 \parallel \text{Li}_4\text{Ti}_5\text{O}_{12}$ pouch cells. **a, b**, Cycling performance of $\text{LiMn}_2\text{O}_4 \parallel \text{Li}_4\text{Ti}_5\text{O}_{12}$ pouch cells with an areal capacity of 1.5 mAh cm^{-2} (**a**) and 2.5 mAh cm^{-2} (**b**) in 4.5 m electrolyte at 1C . **c**, Cycling performance of $\text{Li}_{1.5}\text{Mn}_2\text{O}_4 \parallel \text{Li}_4\text{Ti}_5\text{O}_{12}$ pouch cells with an areal capacity of 2.5 mAh cm^{-2} in 4.5 m electrolyte at 1C . **d**, Comparison of the electrolyte stability window of typical aqueous electrolytes with different salt concentrations (traditional aqueous electrolyte⁴³, 21 m (ref. ¹), 28 m (refs. ^{10,11}) and 63 m (ref. ¹⁵)). **e**, Comparison of 4.5 m electrolyte-based aqueous Li-ion batteries with other commercialized aqueous electrochemical energy storage technologies as quantified by Supplementary Table 6.

Conclusion

In summary, beyond 21 m WISE with a stability window of 3.0 V , we developed a 4.5 m $\text{LiTFSI-KOH-CO(NH}_2)_2\text{-H}_2\text{O}$ electrolyte with an expanded electrochemical stability window of 3.3 V . This was achieved by adding non-flammable $\text{CO(NH}_2)_2$ to replace LiTFSI and further reducing the number of H_2O in the Li^+ solvation shell from 2.6 in WISE to 0.7 . Like the LiTFSI salt, the eutectic $\text{CO(NH}_2)_2$ diluent molecule forms a strong $\text{CO(NH}_2)_2 \cdots \text{H}_2\text{O}$ interaction, subtly substitutes the H_2O site in the Li^+ primary solvation shell and contributes to the formation of a robust SEI consisting of an organic outer layer and a LiF -rich inner layer. The 4.5 m $\text{LiTFSI-KOH-CO(NH}_2)_2\text{-H}_2\text{O}$ electrolyte enables $\text{LiMn}_2\text{O}_4 \parallel \text{Li}_4\text{Ti}_5\text{O}_{12}$ pouch cells with practical settings including thick electrodes (2.5 mAh cm^{-2}) and a low P/N capacity ratio of 1.14 . Superior reversibility over 500 cycles with 72% capacity retention is obtained. Moreover, Li-rich $\text{Li}_{1.5}\text{Mn}_2\text{O}_4$ is further introduced as a lithium reservoir, which releases Li ions during the charging process to compensate for the Li loss in the anode, thereby converting itself into LiMn_2O_4 . This improves the cycling stability (92% capacity retention, 470 cycles) without the introduction of inactive materials. This electrolyte design strategy provides a promising way to expand the electrochemical stability and push aqueous lithium-ion batteries into practical applications where both high safety and low cost are crucial.

Methods

Electrode preparation and electrochemical measurement. The $\text{Li}_4\text{Ti}_5\text{O}_{12}$ anode and LiMn_2O_4 and LiVPO_4F cathode electrodes were provided by Saft Corporation. $\text{Li}_4\text{Ti}_5\text{O}_{12}$ anodes and LiMn_2O_4 cathodes were coated on an Al foil as the current collector: for the 1.5 mAh cm^{-2} cell with P/N ratio of 1.14 , we used 1.5 mAh cm^{-2} $\text{Li}_4\text{Ti}_5\text{O}_{12}$, 1.7 mAh cm^{-2} LiMn_2O_4 and 1.7 mAh cm^{-2} LiVPO_4F . For the 2.5 mAh cm^{-2} cell, we used 2.5 mAh cm^{-2} $\text{Li}_4\text{Ti}_5\text{O}_{12}$ anodes and 2.8 mAh cm^{-2} LiMn_2O_4 cathodes. After calendaring, the porosity was 30% . These electrodes were cut into 1.2 cm^2 sheets and vacuum dried at 80°C for 24 h before assembling. Electrochemical measurements were performed using 2032 coin cells. Whatman glass fibre was used as the separator. As for the pouch cells, aluminium and nickel strips were attached as electrode tabs to the sides of the cathode and anode, respectively. The electrolyte addition for each pouch cell was 3 g Ah^{-1} . The electrolyte was injected into the package, followed by sealing of the battery under vacuum. The linear sweep voltammograms were measured using a three-electrode cell with Pt as a working electrode, Pt as a counter electrode and Ag/AgCl as a reference

electrode. A CHI660B electrochemical workstation was used for the linear sweep voltammogram measurements at a scan speed of 0.2 mV s^{-1} . Galvanostatic cycling of the assembled cells was carried out using a Wuhan LAND Electronic Company CT2001A tester.

Ionic conductivity measurement of aqueous electrolytes. The ionic conductivity was measured with electrochemical impedance spectroscopy using a Gamry workstation (Gamry 1000E, Gamry Instruments), with a 5 mV perturbation and frequency in the range $0.01\text{--}100,000 \text{ Hz}$ at room temperature. The conductivity cell constants were predetermined using 0.01 M aqueous KCl standard solution at room temperature.

Sample characterization. Raman spectra were collected with a Horiba Jobin Yvon Labram Aramis using a 532 nm diode-pumped solid-state laser, with all the samples sealed in a test glass tube. The individual $\text{CO(NH}_2)_2$ and H_2O , $\text{CO(NH}_2)_2\text{-H}_2\text{O}$ ($0.4:1$) eutectic electrolyte and 21 m WISE were used as references, which is in accordance with data in the literature. The FTIR was recorded by a NEXUS 670 FTIR instrument. The ^{17}O NMR spectra were acquired on a Bruker DRX 500 spectrometer at a ^{17}O frequency of 67.81 MHz , using the chemical shift of the ^{17}O nucleus in pure water as the 0 ppm reference. All NMR measurements were conducted at 296.2 K . XPS experiments were carried out on a high-resolution Kratos AXIS 165 X-ray photoelectron spectrometer using monochromatic $\text{Al K}\alpha$ radiation. All the samples were recovered from the full aqueous Li-ion battery cell after electrochemical cyclings. The samples were washed and then dried under vacuum for two hours before XPS measurement. The morphologies of the samples were observed on a JEOL-JEM 2100F transmission electron microscope (100 kV) and a Hitachi SU-70 field emission scanning electron microscope (5 kV).

Molecular dynamics simulations. Molecular dynamics simulations were used to explore the solvation structure of the electrolytes (Supplementary Note 7).

Data availability

The data supporting the findings of this study are available within the article and its Supplementary Information files.

Received: 12 August 2020; Accepted: 23 December 2021;

Published online: 07 February 2022

References

- Suo, L. et al. “Water-in-salt” electrolyte enables high-voltage aqueous lithium-ion chemistries. *Science* **350**, 938–943 (2015).
- Ueno, K. et al. Glyme–lithium salt equimolar molten mixtures: concentrated solutions or solvate ionic liquids? *J. Phys. Chem. B* **116**, 11323–11331 (2012).

3. Wang, J. et al. Superconcentrated electrolytes for a high-voltage lithium-ion battery. *Nat. Commun.* **7**, 12032 (2016).
4. Borodin, O., Self, J., Persson, K. A., Wang, C. & Xu, K. Uncharted waters: super-concentrated electrolytes. *Joule* **4**, 69–100 (2020).
5. Jiao, S. et al. Stable cycling of high-voltage lithium metal batteries in ether electrolytes. *Nat. Energy* **3**, 739–746 (2018).
6. Cao, Z., Hashinokuchi, M., Doi, T. & Inaba, M. Improved cycle performance of $\text{LiNi}_{0.8}\text{Co}_{0.1}\text{Mn}_{0.1}\text{O}_2$ positive electrode material in highly concentrated LiBF_4/DMC . *J. Electrochem. Soc.* **166**, A82–A88 (2019).
7. Chen, S. et al. High-voltage lithium-metal batteries enabled by localized high-concentration electrolytes. *Adv. Mater.* **30**, 1706102 (2018).
8. Cao, X. et al. Monolithic solid–electrolyte interphases formed in fluorinated orthoformate-based electrolytes minimize Li depletion and pulverization. *Nat. Energy* **4**, 796–805 (2019).
9. Fan, X. et al. Non-flammable electrolyte enables Li-metal batteries with aggressive cathode chemistries. *Nat. Nanotechnol.* **13**, 715–722 (2018).
10. Yamada, Y. et al. Hydrate-melt electrolytes for high-energy-density aqueous batteries. *Nat. Energy* **1**, 16129 (2016).
11. Suo, L. et al. Advanced high-voltage aqueous lithium-ion battery enabled by “water-in-bisalt” electrolyte. *Angew. Chem. Int. Ed.* **55**, 7136–7141 (2016).
12. Wang, F. et al. Spinel $\text{LiNi}_{0.5}\text{Mn}_{1.5}\text{O}_4$ cathode for high-energy aqueous lithium-ion batteries. *Adv. Energy Mater.* **7**, 1600922 (2017).
13. Lukatskaya, M. R. et al. Concentrated mixed cation acetate “water-in-salt” solutions as green and low-cost high voltage electrolytes for aqueous batteries. *Energy Environ. Sci.* **11**, 2876–2883 (2018).
14. Ko, S. et al. Lithium-salt monohydrate melt: a stable electrolyte for aqueous lithium-ion batteries. *Electrochem. Commun.* **104**, 106488 (2019).
15. Chen, L. et al. A 63 m superconcentrated aqueous electrolyte for high-energy Li-ion batteries. *ACS Energy Lett.* **5**, 968–974 (2020).
16. Drognet, L., Grimaud, A., Fontaine, O. & Tarascon, J. M. Water-in-salt electrolyte (WiSE) for aqueous batteries: a long way to practicality. *Adv. Energy Mater.* **10**, 2002440 (2020).
17. Wang, F. et al. Hybrid aqueous/non-aqueous electrolyte for safe and high-energy Li-ion batteries. *Joule* **2**, 927–937 (2018).
18. Chen, J. et al. Improving electrochemical stability and low-temperature performance with water/acetonitrile hybrid electrolytes. *Adv. Energy Mater.* **10**, 1902654 (2020).
19. Yang, C. et al. 4.0 V aqueous Li-ion batteries. *Joule* **1**, 122–132 (2017).
20. He, X. et al. Fluorine-free water-in-ionomer electrolytes for sustainable lithium-ion batteries. *Nat. Commun.* **9**, 5320 (2018).
21. Xie, J., Liang, Z. & Lu, Y.-C. Molecular crowding electrolytes for high-voltage aqueous batteries. *Nat. Mater.* **19**, 1006–1011 (2020).
22. Dubouis, N. et al. The role of the hydrogen evolution reaction in the solid–electrolyte interphase formation mechanism for “water-in-salt” electrolytes. *Energy Environ. Sci.* **11**, 3491–3499 (2018).
23. Cordeiro, J. M. M. & Freitas, L. C. G. Study of water and dimethylformamide interaction by computer simulation. *Z. Naturforsch. A* **54**, 110–116 (1999).
24. Qiu, H. et al. Zinc anode-compatible in-situ solid electrolyte interphase via cation solvation modulation. *Nat. Commun.* **10**, 5374 (2019).
25. Zhao, J. et al. “Water-in-deep eutectic solvent” electrolytes enable zinc metal anodes for rechargeable aqueous batteries. *Nano Energy* **57**, 625–634 (2019).
26. Hu, Z. et al. Nonflammable nitrile deep eutectic electrolyte enables high-voltage lithium metal batteries. *Chem. Mater.* **8**, 3405–3413 (2020).
27. Rousseau, B., Alsenoy, C. V., Keuleers, R. & Desseyn, H. Solids modeled by ab-initio crystal field methods. Part 17. Study of the structure and vibrational spectrum of urea in the gas phase and in its $P4_2/m$ crystal phase. *J. Phys. Chem. A* **102**, 6540–6548 (1998).
28. Araujo, C. et al. Inelastic neutron scattering study of relin: shedding light on the hydrogen bonding network of deep eutectic solvents. *Phys. Chem. Chem. Phys.* **19**, 17998–18009 (2017).
29. Keuleers, R., Desseyn, H., Rousseau, B. & Alsenoy, C. V. Vibrational analysis of urea. *J. Phys. Chem. A* **103**, 4621–4630 (1999).
30. Finer, E., Franks, F. & Tait, M. Nuclear magnetic resonance studies of aqueous urea solutions. *J. Am. Chem. Soc.* **94**, 4424–4429 (1972).
31. Sim, L., Yahya, R. & Arof, A. Infrared studies of polyacrylonitrile-based polymer electrolytes incorporated with lithium bis (trifluoromethane) sulfonimide and urea as deep eutectic solvent. *Opt. Mater.* **56**, 140–144 (2016).
32. Zhu, B., Liang, Z. & Zou, R. Designing advanced catalysts for energy conversion based on urea oxidation reaction. *Small* **16**, 1906133 (2020).
33. Xu, J. et al. Conductive carbon nitride for excellent energy storage. *Adv. Mater.* **29**, 1701674 (2017).
34. Beamson, G. & Briggs, D. *High Resolution XPS of Organic Polymers, the Scienta ESCA300 Database* (Wiley, 1992).
35. Shaw, W. H. & Bordeaux, J. J. The decomposition of urea in aqueous media. *J. Am. Chem. Soc.* **77**, 4729–4733 (1955).
36. Hou, Z. et al. Formation of solid–electrolyte interfaces in aqueous electrolytes by altering cation-solvation shell structure. *Adv. Energy Mater.* **10**, 1903665 (2020).
37. Violante de Paz Bañez, M., Aznar Moreno, J. A. & Galbis, J. A. Versatile sugar derivatives for the synthesis of potential degradable hydrophilic-hydrophobic polyurethanes and polyureas. *J. Carbohydr. Chem.* **27**, 120–140 (2008).
38. Chen, J. et al. Electrolyte design for LiF-rich solid–electrolyte interfaces to enable high-performance micro-sized alloy anodes for batteries. *Nat. Energy* **5**, 386–397 (2020).
39. Smith, A., Burns, J. C., Zhao, X., Xiong, D. & Dahn, J. A high precision coulometry study of the SEI growth in Li/graphite cells. *J. Electrochem. Soc.* **158**, A447–A452 (2011).
40. Diaz-Lopez, M. et al. Li_2O : Li–Mn–O disordered rock-salt nanocomposites as cathode prelithiation additives for high-energy density Li-ion batteries. *Adv. Energy Mater.* **10**, 1902788 (2020).
41. Betz, J. et al. Theoretical versus practical energy: a plea for more transparency in the energy calculation of different rechargeable battery systems. *Adv. Energy Mater.* **9**, 1803170 (2019).
42. Chao, D. et al. Roadmap for advanced aqueous batteries: from design of materials to applications. *Sci. Adv.* **6**, eaba4098 (2020).
43. Manalastas, W. Jr et al. Water in rechargeable multivalent-ion batteries: an electrochemical Pandora’s box. *ChemSusChem* **12**, 379–396 (2019).

Acknowledgements

This work was financially supported by the US Department of Energy ARPA-E grant DEAR0000389.

Author contributions

J.X. and C.W. conceived the idea for the project. J.X., J.Z. and C.Y. prepared the materials and performed the electrochemical experiments. X.J. conducted the quantum chemistry calculations and molecular dynamics simulations. J.X., P.W. and S.L. conducted the characterizations. K.L. and P.K. completed the differential scanning calorimetry tests. F.C. performed the NMR measurements. All the authors discussed the results, analysed the data and drafted the manuscript.

Competing interests

J.X., X.J. and C.H. are inventors on the US patent application (application number 2021-158-1) filed by the University of Maryland regarding the electrolytes described in this Article.

Additional information

Supplementary information The online version contains supplementary material available at <https://doi.org/10.1038/s41560-021-00977-5>.

Correspondence and requests for materials should be addressed to Chunsheng Wang.

Peer review information *Nature Energy* thanks Maria Lukatskaya and the other, anonymous, reviewer(s) for their contribution to the peer review of this work.

Reprints and permissions information is available at www.nature.com/reprints.

Publisher’s note Springer Nature remains neutral with regard to jurisdictional claims in published maps and institutional affiliations.

© The Author(s), under exclusive licence to Springer Nature Limited 2022